

Robust and Broadband Optical Coupling by Topological Waveguide Arrays

Wange Song, Wenzhao Sun, Chen Chen, Qinghai Song, Shumin Xiao,* Shining Zhu, and Tao Li*

Photonic topological states have been exploited to give rise to robust optical behaviors that are quite insensitive to local defects or perturbations, which provide a promising solution for robust photonic integrations. Specifically, for example, optical coupling between waveguides is a universal function in integrated photonics. However, the coupling performance usually suffers from high structure-sensitivity and challenges current manufacturing for massive production. Here, the topological edge state in a finite Su–Schrieffer–Heeger modeled optical waveguide array is explored and robust optical coupling (e.g., directional coupling and beam splitting) is demonstrated, which is quite insensitive to structural variations. It is experimentally proved that even a large discrepancy (21–26% structural deviation) in silicon waveguides gaps has little influence on optical coupling (>90% performance), while conventional counterparts totally break down. Moreover, thanks to such a topological design, the devices show much broader working bandwidth (≈ 10 times performance improvement) than the conventional ones, greatly favoring the photonic integrations. This work would inspire new families of optical devices with robust and broadband properties that can excite more interesting and useful exploration in both fields, and possibly open a new avenue toward topological devices with unique properties and functionalities.

1. Introduction

Topological photonics has arrested a great deal of interest with intriguing optical phenomena associated with the topological edge states (TESs).^[1–6] Non-trivial TESs have been well revealed in two-dimensional (2D) photonic topological insulators, which demonstrated very good robustness to structural defects or scatterers with one-way propagations.^[1,2] There are also 1D topological systems that have edge states that exist at the termination of a 1D lattice. For example, zero modes in the Su–Schrieffer–Heeger (SSH) model^[7,8] have gained significant attention and have been explored in many different systems.^[4,9–16] All the progress in fundamental researches of topological photonics has recently prompted great efforts to design robust optical devices that are insensitive to structural perturbations and fabrication disorders. For example, topological properties have been used to create robust optical delay lines,^[17] polarization conversion,^[18,19] non-linear light

generation,^[20] and even the topological insulator laser.^[13,16,21,22] This robust topological design suggests a promising application for integrated photonics.^[23–31]

Integrated photonic devices with coupled waveguides usually exhibit high structure-sensitive performance. Therefore, precise requirement in micro/nanofabrication is very stringent, which severely challenges current manufacturing technology. Great efforts have been made to solve the longstanding problem, such as compensation process by Mach–Zehnder interferometer,^[32] programmable solution for on-demand fabrications,^[33] and adiabatic passage designs.^[34–37] These approaches usually require external intervention or strict parameter condition that have to sacrifice in some other important aspects,^[32–37] and there is still a high demand for devices with a naturally robust design. More recently, the robust waveguiding and transportation based on TES have been proposed and demonstrated in silicon platform,^[9,38,39] showing the advantages of topological design in integrated photonic devices. Therefore, it is quite possible to utilize these TESs to access the robust coupling of light between waveguides, though they were rarely studied previously.

Here, we investigated the coupling property of topological edge states in finite SSH modeled waveguide arrays, which were found

W. Song, C. Chen, Prof. S. Zhu, Prof. T. Li
National Laboratory of Solid State Microstructures
Key Laboratory of Intelligent Optical Sensing and Integration
Jiangsu Key Laboratory of Artificial Functional Materials
College of Engineering and Applied Sciences
Nanjing University
Nanjing 210093, China
E-mail: taoli@nju.edu.cn

W. Sun, Prof. Q. Song, Prof. S. Xiao
State Key Laboratory on Tunable Laser Technology
Ministry of Industry and Information Technology
Key Lab of Micro-Nano Optoelectronic Information System
Shenzhen Graduate School
Harbin Institute of Technology
Shenzhen 518055, China
E-mail: shumin.xiao@hit.edu.cn

W. Song, C. Chen, Prof. S. Zhu, Prof. T. Li
Collaborative Innovation Center of Advanced Microstructures
Nanjing 210093, China

 The ORCID identification number(s) for the author(s) of this article can be found under <https://doi.org/10.1002/lpor.201900193>

DOI: 10.1002/lpor.201900193

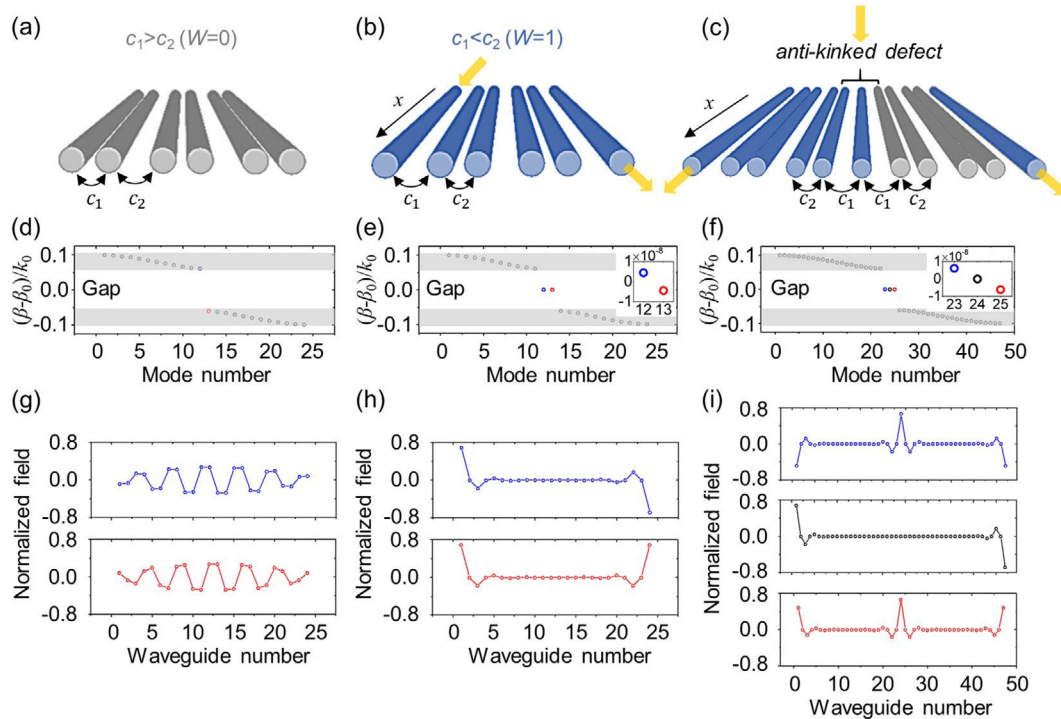


Figure 1. Design of topological waveguide array. Schematics of 1D SSH model of a) trivial topological structure, and nontrivial topological ones for b) directional coupling and c) beam splitting. d–f) Band structure associated with the three configurations. k_0 is the wave vector in free space. Gray areas indicate the bulk bands. Inset figures in (e) and (f) are the zoom-in pictures of the discrete modes inside the bandgap. g–i) Distribution of the wavefunction of certain eigenmodes in the waveguide array indicated by the corresponding colors.

to give rise to robust optical coupling functionalities (e.g., directional coupling and beam splitting) that are immune to structural variations to certain degrees. These optical devices were successfully implemented in silicon waveguides, and the robustness was verified by comparing the samples with those of intentionally introduced discrepancies. More interestingly, this topological design further gives rise to broadband property of the coupling process, which is quite favorable in the on-chip photonic integrations. Both the robustness and broadband properties are experimentally confirmed by comparisons with the conventional counterparts, showing the performances of our devices are quite insensitive to structural variation and wavelength. Our designs have shown significant advantages with loose fabrication requirement that would possibly pave the way in massive photonic integrations.

2. Results

2.1. Coupling of Topological States in a Finite SSH Model

We would like to start from an SSH model defined by a coupled optical waveguide array with alternating coupling strengths in neighbor (like a dimer chain). The optical field propagation within the waveguide array can be described by the coupled-mode theory (CMT) in the tight-binding approximation^[11]

$$\begin{aligned} -i \frac{\partial}{\partial x} \varphi_n &= \beta_0 \varphi_n + c_2 \varphi_{n-1} + c_1 \varphi_{n+1}, \quad n = 1, 3, \dots \\ -i \frac{\partial}{\partial x} \varphi_n &= \beta_0 \varphi_n + c_1 \varphi_{n-1} + c_2 \varphi_{n+1}, \quad n = 2, 4, \dots \end{aligned} \quad (1)$$

where n enumerates the waveguides, with $n = 1, 2, 3, \dots, N$, φ_n denotes the optical field in the n th waveguide, β_0 is the propagation constant of the isolated waveguide, c_1 and c_2 denote the alternating coupling coefficients in neighbor, and the magnitude of the difference $\delta = |c_2 - c_1|$ is referred to as the dimerization.^[12] The corresponding Hamiltonian writes^[13]

$$H(k) = \begin{pmatrix} 0 & \rho^*(k) \\ \rho(k) & 0 \end{pmatrix} \quad (2)$$

where $\rho(k) = c_1 + c_2 \exp(ika)$ (here the term of $\exp(ika)$ is the contribution of Bloch wave). The Hamiltonian $H(k)$ possesses a chiral symmetry defined by the Pauli matrix σ_z (i.e., $\sigma_z H(k) \sigma_z = -H(k)$). The principal consequence of this symmetry is that the energy spectrum is symmetric around the zero energy.^[13] The Hamiltonian $H(k)$ exhibits two topologically distinct phases associated with the two possible dimerizations $c_1 > c_2$ (topologically trivial phase) and $c_1 < c_2$ (topologically nontrivial phase) as shown in Figure 1a,b, respectively. In fact, these two different topological phases can be distinguished by the Zak phase or winding number W .^[12,40] Here, W is equivalent to the Zak phase,^[41] up to a factor of π . The winding number can be calculated by $W = \frac{i}{\pi} \oint_{\text{BZ}} dk \langle \psi(k) | \frac{\partial}{\partial k} | \psi(k) \rangle$ (where $|\psi(k)\rangle$ is Bloch wave functions^[9,41]), which takes on the value of 0 when $c_1 > c_2$ and 1 when $c_1 < c_2$. Non-zero winding number implies nontrivial topology and indicates the existence of edge states. The eigenstates of $H(k)$ form two bands (\pm) in momentum space separated by a gap of magnitude 2δ , as the mode diagrams calculated for an array of 24 waveguides exhibiting $W = 0$ and $W = 1$ displayed in

Figure 1d,e, respectively. The most notable difference is the existence in the latter case of two states (indicated by the blue and red circles) in the midgap corresponding to a pair of topological edge states.

It should be noted that the mode constants (i.e., propagation constant) of these two TESs (β_{TES1} and β_{TES2}) are not exactly equal to zero, while slightly split due to the coupling between the two boundaries according to the finite waveguide number.^[42] Such kinds of coupling caused near-zero mode of TESs have been demonstrated in finite topological systems, for example, zigzag chains of plasmonic and dielectric nanoparticles.^[13,14,43] The field distributions of the two TESs are presented in Figure 1h, from which strong field localizations at the boundaries in symmetric and asymmetric manners are observed that confirms the presence of TES (as a comparison, two extended eigenstates with the same mode number with $W = 0$ are displayed in Figure 1g, showing two bulk modes). If the input state is a superposition of the two TESs, the beating effect will give rise to a periodic field energy transfer between the two boundaries, which indicates the potential functionality of directional coupling. We would like to define this structure as the directional coupler (DC). The coupling strength κ of two boundaries can be defined according to the splitting of the mode constants of the pair of TESs as $\kappa_{\text{DC}} = (\beta_{\text{TES1}} - \beta_{\text{TES2}})/2$, which is related to system size (waveguide number N) and the dimerization (δ). It is evident that κ decreases as N and δ increase (Section S1, Supporting Information). In Figure 1c, we combine two dimers together with opposite configurations (with topologically nontrivial phase on the left and topologically trivial phase on the right), and there forms an interface with two weak couplings (also known as antikinked defect^[11]). A topological transition from $W = 1$ to $W = 0$ occurs right at the interface. As expected, there are three topological states in the midgap. One is an exact zero mode, and the other two slightly separate with both localizations at the interface and boundaries simultaneously, as shown in Figure 1f,i. **Interestingly, the beat of the two near-zero modes (blue and red ones, with mode constant β_{TES1} and β_{TES3}) leads to periodic energy transfer from the center to the two boundaries, which can work as the optical beam splitter (BS). The coupling strength of the center and the boundaries is defined as $\kappa_{\text{BS}} = (\beta_{\text{TES1}} - \beta_{\text{TES3}})/2$, and κ decreases as N and δ increase as well as the DC case (Section S1, Supporting Information).**

2.2. Robustness of Topological States

Since the TESs rightly locate inside the bandgap, they are topologically protected by the chiral symmetry,^[15] which should enable the DC and BS to work in a robust manner that will be seldom affected by the structural fluctuations on the coupling strengths. To characterize the topological protection property of the coupling phenomenon, we intentionally introduce the fluctuations in gap sizes among the waveguide array corresponding to random modifications of the coupling strengths. They are defined in the forms of^[12]

$$\begin{aligned} c_1^{i'} &= c_1 + \frac{R}{2} \xi_i (c_2 - c_1) \\ c_2^{i'} &= c_2 - \frac{R}{2} \xi_i (c_2 - c_1) \end{aligned} \quad (3)$$

where ξ_i is the distributed random number in the interval $[-1, 1]$ modulating the coupling between the i th and $(i+1)$ th waveguides, and they are independent of each other. R is the fluctuation strength varying from 0 to 1. Variation of coupling coefficients defined by Equation (3) only modify the off-diagonal terms (i.e., c_1 and c_2) in Hamiltonian of Equation (1) and thus do not change the chiral symmetry.^[13] Consequently, the eigen zero modes are immune to such fluctuations. Although the TESs in the finite system are not the exact zero modes, their mode constants are very close to zero, which still guarantee the topological protection of the chiral symmetry against certain fluctuations.^[42,43] **Figure 2** shows the evolution of the propagation constant of the edge state as a function of the fluctuation strength with different waveguide numbers at fixed dimerizations ($\delta/k_0 = 0.017$) in the configurations of DC (Figure 2a–c) and BS (Figure 2d–f). It is clear that the fluctuation of two splitting TESs in DC grows with the R increases and tends to get larger as the waveguide number decreases, while it still keeps good location inside the bandgap even for the $N = 6$ case (Figure 2c), indicating the topological protection is well preserved for these modes. It is the same case for the BS ones. These TES modes are well isolated from the bulk bands would quite possibly enable the robust DC and BS functionalities.

2.3. Topological Designs of Coupling Devices

According to above considerations, we proposed the silicon waveguide arrays for DC and BS functionalities, as shown in **Figure 3a**. Each element of the dimer waveguide array is a silicon waveguide with refractive index $n_{\text{Si}} = 3.48$ at 1550 nm, waveguide width $w = 400$ nm and height $h = 220$ nm, which are designed on a sapphire substrate ($n_{\text{Al}_2\text{O}_3} = 1.75$) and in the air background. In the waveguides, only one fundamental mode is supported in the silicon waveguide at $\lambda = 1550$ nm with a propagation constant of $\beta_0 = 2.16k_0$ ($k_0 = 2\pi/\lambda$ is the wave vector in free space). Here, we fixed the total number of waveguides to $N = 6$ and $N = 11$ for topological DC and BS structures, respectively. The gaps between waveguides are chosen to be $d_1 = 200$ nm and $d_2 = 120$ nm, corresponding to $c_1/k_0 = 0.020$, $c_2/k_0 = 0.037$, and $\delta/k_0 = 0.017$, which give rise to coupling lengths of $L_{\text{DC}} = 89.70 \mu\text{m}$ and $L_{\text{BS}} = 70.60 \mu\text{m}$ (Section S1, Supporting Information). To reflect the structural variation, a normalized deviation degree $\eta = \text{Max}\{|\Delta d_i|/d_i\}$ ($\Delta d_i = |d_i' - d_i|$, where d_i and d_i' are the ideal and actual gap distances) is used to define the structural discrepancy. The η can be derived from the fluctuation strength (R) according to the relation between the coupling coefficient and gap distance (Figure S1a, Supporting Information). To check the robust behavior of topological structures, a conventional DC/BS with two/three waveguides separated with a certain distance was also investigated for comparison, as illustrated in Figure 3b. Its coupling length is designed to be equal to that of the topological DC/BS structure.

A commercial finite-element analysis solver (Comsol Multiphysics 5.3) was employed for full-wave simulations. The propagation of the optical field within 100 μm long silicon waveguides of topological DC and BS structures are shown in Figure 3c,e, respectively, with the exact superposition mode as the

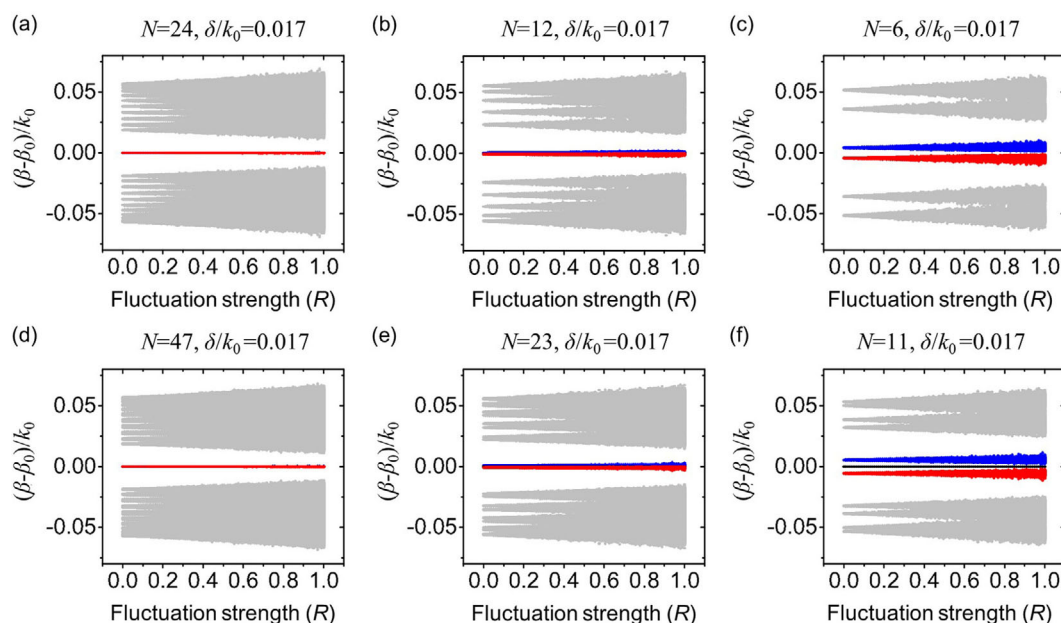


Figure 2. The influences of fluctuation strength on the topological band structure. a–c) Evolution of the propagation constant of the topological edge state as a function of the fluctuation strength for topological DC structures. a) $N = 24$, $\delta/k_0 = 0.017$. b) $N = 12$, $\delta/k_0 = 0.017$. c) $N = 6$, $\delta/k_0 = 0.017$. d–f) The corresponding results for topological BS structures. d) $N = 47$, $\delta/k_0 = 0.017$. e) $N = 23$, $\delta/k_0 = 0.017$. f) $N = 11$, $\delta/k_0 = 0.017$. Gray areas indicate the width of the bands.

input. It is observed that the field transfers between the boundaries/interface, and the coupling lengths are about 85 and 75 μm for DC and BS, respectively, which are in good agreement with our CMT calculations. Next, structural discrepancies were introduced with random waveguide separations, which are termed as controlled devices. It is clearly seen that the performances (including coupling efficiency and extinction ratio) of directional coupling and beam splitting are preserved quite well for the controlled samples ($\eta = 13$ and 20%), showing good immunity against the structural variations. However, for the conventional counterparts, the increasing fluctuations greatly degrade the performance of the devices with obvious changes in the target outputs, and even make their functions break down for the $\eta = 20\%$ case (Figure 3d,f). As for the coupling efficiency, according to our simulations we obtained similar data of 90.4% for the topological DC and 93.3% for the conventional one in ideal cases (from Figure 3c,d with $\eta = 0$).

2.4. Experimental Results

The experimental samples are fabricated in a silicon wafer on sapphire substrate using E-beam lithography with hydrogen silsesquioxane (HSQ) photoresist and an inductively-coupled plasma (ICP) etching process (see Section 4), which includes the waveguide array and several extended grating couplers. The lengths of the waveguide arrays are 100 and 80 μm for the DC and BS devices, respectively. The scanning electron microscopy (SEM) images of the fabricated devices are shown in Figure 4. The input/output ports are connected to grating couplers from the end of waveguide array by certain waveguides. The coupling in and out processes can be clearly imaged by a near-infrared

(NIR) camera (Xenics Xeva 1083) through a microscope objective (see Section 4). In experiments, we input the light into the boundary waveguide in the DC device and center waveguide in BS by focusing the laser ($\lambda = 1550$ nm) to port I_1 (Figure 4a,b). The transmitted signals can be measured from the output ports (O_1 and O_2 for DC, O_2 , O_1 , and O_3 for BS).

To quantitatively evaluate the performances of DC and BS devices, we define a coupling ratio as $CR = I_{O2}/(I_{O1} + I_{O2})$ for DC and $CR = (I_{O2} + I_{O3})/(I_{O1} + I_{O2} + I_{O3})$ for BS devices, where I_{O_i} refers to the measured intensity from port O_i . The design of controlled samples with randomly introduced discrepancies is provided in Section S2, Supporting Information. Figure 5a,b shows the experimental data of coupling ratios for the topological and conventional devices with respect to different structural deviation degree η (which can also be referenced by the maximum deviation value of gap distance, as shown in Figure S3, Supporting Information). It should be noted that each data is averaged from three samples (Figure S4, Supporting Information) with the same structural deviation degree, and the error bar indicates the influence of the random deviations introduced in nanofabrications. It is clearly observed that CR of topological DC keeps a high value (>90%) in a considerably large structural discrepancy ($\eta = 16.7\%$), while the conventional device even loses its coupling function when η reaches 9.8%. The oscillation feature of the CR value with respect to η of the conventional DC case attributes to the coupling reverse with the coupling strength changes. As for the BS case, the CR remains 90% even for $\eta = 25\%$ for the topological device, while conventional one reaches to the minimum only when $\eta = 4.6\%$. Figure 5c,d displays the topological DC and BS devices with ideal and controlled parameters ($\eta = 0$, 8.3%, and 16.7%, from top to bottom), respectively. It is clear that there are bright spots from the expected output ports (O_2 for DC, O_2

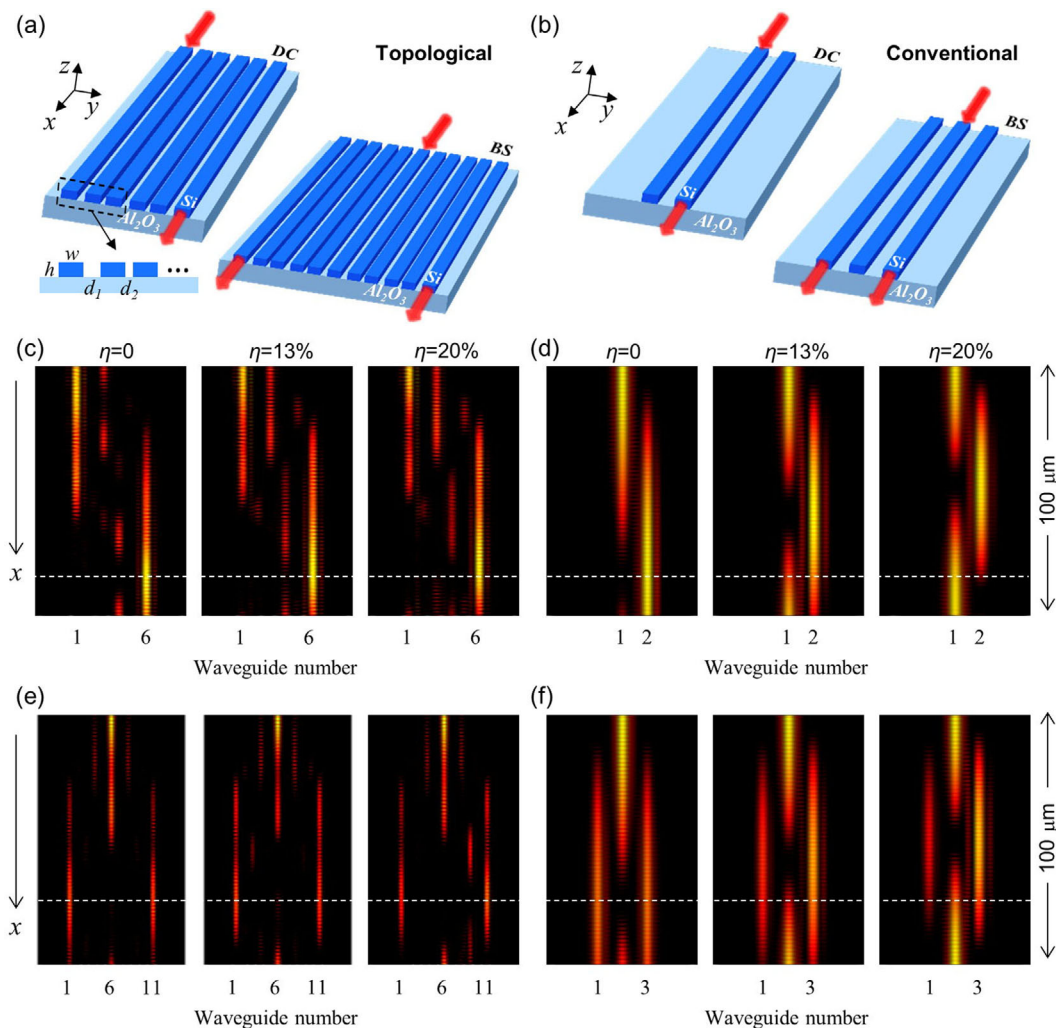


Figure 3. Topological DC and BS devices and comparisons to the conventional ones in silicon waveguides. Schematics of the structures of a) topological DC and BS by Silicon waveguide arrays and b) conventional DC and BS with directly coupled waveguides. Simulated optical field propagations in the structures of c) topological DC, d) conventional DC, e) topological BS, and f) conventional BS with different structural deviation degree $\eta = 0, 13\%, 20\%$.

and O_3 for BS) for all three samples showing excellent DC and BS functions, in which the controlled samples are almost unaffected by the structural discrepancies. However, for cases of conventional DC and BS, we find the output signal deviates from the preferred output ports greatly as the discrepancies are introduced (Figure 5e,f) with their structural deviations marked out. Note that the device lengths of the conventional DC and BS samples are designed and fabricated as same as the arrayed samples ($100 \mu\text{m}$ for DC and $80 \mu\text{m}$ for BS). This comparison results definitely confirm the topological devices are quite robust against the structural variations.

Moreover, we significantly find that our topological design for optical coupling is also considerably insensitive to the working wavelengths that indicates a broadband property. This insensitive can be intuitively explained that the coupling of two boundaries is mainly related to the dimerization $\delta = |c_2 - c_1|$, which can be stable as wavelength changes because the c_1 and c_2 follow the same trend of change. To verify this, further experiments were

performed on the topological and conventional DC devices with respect to different wavelengths (see Section 4) and the results are shown in Figure 6. Expectedly, the topological devices (here we choose the no artificial deviation samples $\eta = 0$) have broader bandwidth ($\approx 100 \text{ nm}$) than conventional counterparts ($\approx 10 \text{ nm}$) for a coupling ratio of $> 90\%$, showing ≈ 10 times performance improvement. Note that in our experiments as the wavelength deviates from the center wavelength, the detected output intensity decreases. It is due to the input/output efficiency decreases for the mismatch between light and grating coupler, since all grating couplers (Figure 4e) are particularly designed for 1550 nm wavelength. Nevertheless, it does not affect the DC performances. As for the conventional DC device, although the preliminary designed working wavelength is 1550 nm , the maximum coupling ratio shifts to 1560 nm (Figure 6a) due to uncontrollable discrepancies in fabricated samples. In this sense, the structural sensitive property of conventional design will greatly degrade the DC function at a preferred working wavelength. Since the

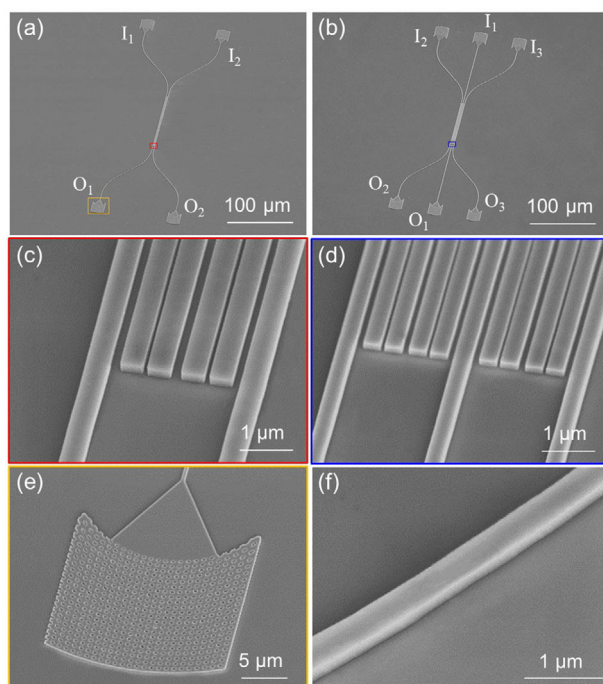


Figure 4. Structures of the topological devices. SEM pictures of the fabricated topological a) DC and b) BS devices, where the input/output waveguides have grating couplers at their ends. The lengths of the silicon waveguides are 100 and 80 μm , respectively. e, f) Zoom-in SEM view of the devices. c, d) The ends of the waveguide arrays for c) DC and for d) BS. e) One of the grating couplers. f) Silicon waveguide.

working bandwidth is a very important index in photonic integrations and the broadband coupler has always been the pursuit of people working in this field, this topological waveguide array promises a brand new strategy for broadband photonic designs.

Additionally, it should be mentioned that the input/output ports in our experiments are all connected to a single waveguide from the array, so that the input mode is not the exact superposition mode of the coupled TESs. To check the influence of input mode, we carefully prepared the exact state by engineering the intensities and phases of two waveguides on the boundary (one straight waveguide together with a curved branch). The detailed structure design, fabrication, and optical coupling results are provided in Section S3, Supporting Information. It comes to similar good robust performances as we demonstrated in Figure 5, which indicates the strict mode preparation is not very necessary. It attributes to the fact that these TESs have strong field confinement at single waveguide in spite of some extension to others. The single-waveguide input has been proved to be of the major properties of TES modes, and can work well with robust optical coupling functions. In all these experiments, we face an on-site disorder of $\approx 3\%$ (12 nm) in the values of w introduced in fabrication.

3. Conclusion

So far, we have developed and confirmed that the topologically arrayed devices have robust and broadband properties for the con-

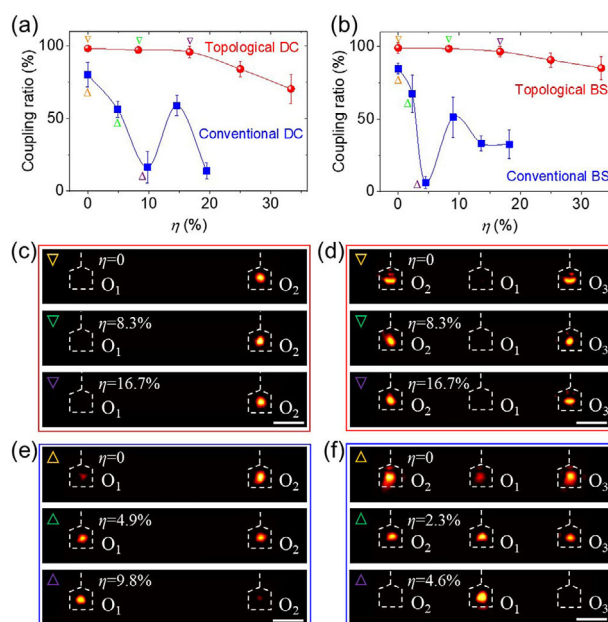


Figure 5. Experimental demonstration of topological DC and BS. The coupling ratio as a function of structural deviation degree (η) for a) topological and conventional DC devices, b) topological and conventional BS devices. Each data is averaged from three samples with the same structural deviation degree, and the error bar indicates the influence of the random deviations introduced in nanofabrications. Experimentally captured output signals of c) topological DC and d) topological BS devices indicated by inverted triangles in (a) and (b). Top: Ideal device ($\eta = 0$). Middle: Controlled device with $\eta = 8.3\%$. Bottom: Controlled device with $\eta = 16.7\%$. e, f) The experimental results of conventional DC and BS devices indicated by triangles in (a) and (b) with their deviation degree (η) marked out. Scale bar = 20 μm .

structed directional coupling and beam splitting functions. On the other hand, they inevitably have larger footprint compared with conventional counterparts. Indeed, a smaller footprint with robust performance is definitely most favorable. However, they are quite difficult to access at the same time in our scheme except for some other designs also with sacrifices.^[32,33] According to our work, further downsizing footprints will inevitably weaken the robustness, and there is a trade-off between the robust performance and small footprint. Actually, it is the common feature also for other robust and broadband approaches of DC and BS,^[34,35] but the footprint of our topological design is much smaller than previous adiabatic design,^[36,37] and there are still spaces in optimization. However, in this work, we would emphasize the importance of the robustness, which would probably overtake the fabrication challenge in massive photonic integrations and seem more critical than the compact requirement currently.

In summary, we designed and investigated the interesting topological edge states in finite waveguide array with SSH model, which are found to be coupled to some extent that gives rise to robust optical coupling functions. Based on the designs, we significantly demonstrated in experiments, for the first time, the robust photonic integration devices of directional coupler and beam splitter by silicon waveguide array configurations. The functionalities are proved to be insensitive to the variation of waveguides separations and working wavelengths to certain extents, showing

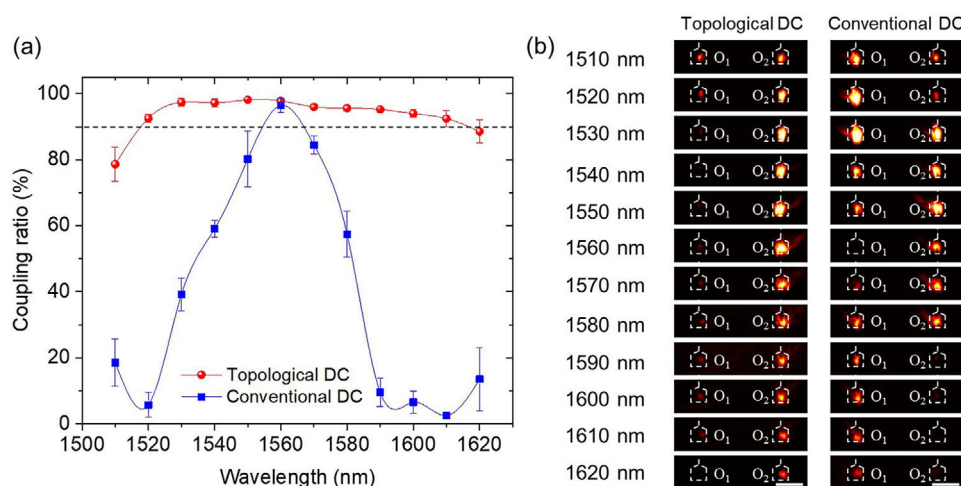


Figure 6. Experimental results of bandwidth for topological and conventional DC. a) The coupling ratio as a function of wavelength for topological and conventional DC devices. Each data is averaged from three samples (without artificial deviation $\eta = 0$) and the error bar indicates the influence of the random deviations introduced in nanofabrications. b) Experimentally captured output signals of topological and conventional DC devices with different wavelengths. Scale bar = 40 μm .

quite good robustness against the structural discrepancies with a broadband performance. All of these priorities are well confirmed by comparing them with conventional devices. Our approach provides a one-time solution that is well compatible with current fabrication process with loose accuracy requirement and broader bandwidth, which would probably boost the progress of massive photonic integrations.

4. Experimental Section

Sample Fabrication: The waveguide arrays and grating nanostructures are fabricated using the method of E-beam lithography and ICP etching process. The substrate used herein is 230 nm silicon deposition on 460 nm alumina substrate, the substrates are cleaned in ultrasound bath in acetone, isopropyl alcohol (IPA), and DI water for 10 min and dried under clean nitrogen flow. Then 100 nm HSQ photoresist film is spin-coated onto the substrate without hotplate bake. After that, the sample is exposed to electron beam in E-beam writer (Raith E-line, 30 kV) and developed to form the HSQ nanostructures. After that, the sample transferred into Oxford instruments plasma technology 380 plasma and etched with C₄F₈ and SF₆ (the flow rates of these two types of gases are 35 sccm:15 sccm). During the etching process, the chamber pressure is stabilized at 15 mTorr, the temperature of the platform is 20 degree, the ICP power is 1200 W, and the RF power is 30 W. After the ICP etching, the HSQ E-beam resist is removed by immersing in hydrofluoric acid (concentration of 8%) for 3 min.

Measurement: In optical measurements, a near-infrared optical wave at the wavelength of 1550 nm from a single frequency mode laser (FL-1550-SF) was focused at the input grating by an objective lens (50 \times), and then coupled into the waveguide mode. The output signals can be detected by the scattering field from the output grating. The coupling-in and -out processes were clearly imaged by a near-infrared (NIR) CCD camera (Xenics Xeva 1083) by transmission scheme through another microscope objective (50 \times). In the broadband measurement, a white light laser (Fianium Supercontinuum, 4 W) with the wavelength range 400–2200 nm was used, and the wavelength was switched by a group of filters (FWHM = 12 nm).

Supporting Information

Supporting Information is available from the Wiley Online Library or from the author.

Acknowledgements

W. Song and W. Sun contributed equally to this work. The authors acknowledge the financial support from The National Key R&D Program of China (2017YFA0303701, 2016YFA0202103), National Natural Science Foundation of China (Nos. 91850204, 11674167, 11621091), and PAPD from Jiangsu province. T.L. thanks the support from Dengfeng Project B of Nanjing University.

Conflict of Interest

The authors declare no conflict of interest.

Keywords

broadband coupling, integrated photonic devices, robust coupling, topological photonics, waveguide arrays

Received: June 7, 2019
Revised: October 30, 2019
Published online: January 13, 2020

- [1] L. Lu, J. D. Joannopoulos, M. Soljačić, *Nat. Photonics* **2014**, *8*, 821.
- [2] T. Ozawa, H. M. Price, A. Amo, N. Goldman, M. Hafezi, L. Lu, M. C. Rechtsman, D. Schuster, J. Simon, O. Zilberberg, I. Carusotto, *Rev. Mod. Phys.* **2019**, *91*, 015006.
- [3] T. Karzig, C.-E. Bardyn, N. H. Lindner, G. Refael, *Phys. Rev. X* **2015**, *5*, 031001.
- [4] Q. Huang, Z. Guo, J. Feng, C. Yu, H. Jiang, Z. Zhang, Z. Wang, H. Chen, *Laser Photonics Rev.* **2019**, 1800339.
- [5] H. Jia, R. Zhang, W. Gao, Q. Guo, B. Yang, J. Hu, Y. Bi, Y. Xiang, C. Liu, S. Zhang, *Science* **2019**, *363*, 148.
- [6] Y. Yang, Z. Gao, H. Xue, L. Zhang, M. He, Z. Yang, R. Singh, Y. Chong, B. Zhang, H. Chen, *Nature* **2019**, *565*, 622.
- [7] W. P. Su, J. R. Schrieffer, A. J. Heeger, *Phys. Rev. Lett.* **1979**, *42*, 1698.

- [8] A. J. Heeger, S. Kivelson, J. Schrieffer, W. P. Su, *Rev. Mod. Phys.* **1988**, 60, 781.
- [9] A. Blanco-Redondo, I. Andonegui, M. J. Collins, G. Harari, Y. Lumer, M. C. Rechtsman, B. J. Eggleton, M. Segev, *Phys. Rev. Lett.* **2016**, 116, 163901.
- [10] T. Kitagawa, M. A. Broome, A. Fedrizzi, M. S. Rudner, E. Berg, I. Kasal, A. Aspuru-Guzik, E. Demler, A. G. White, *Nat. Commun.* **2012**, 3, 882.
- [11] Q. Cheng, Y. Pan, Q. Wang, T. Li, S. Zhu, *Laser Photonics Rev.* **2015**, 9, 392.
- [12] S. Weimann, M. Kremer, Y. Plotnik, Y. Lumer, S. Nolte, K. G. Makris, M. Segev, M. C. Rechtsman, A. Szameit, *Nat. Mater.* **2017**, 16, 433.
- [13] P. St-Jean, V. Goblot, E. Galopin, A. Lemaître, T. Ozawa, L. Le Gratiet, I. Sagnes, J. Bloch, A. Amo, *Nat. Photonics* **2017**, 11, 651.
- [14] A. P. Slobozhanyuk, A. N. Poddubny, A. E. Miroshnichenko, P. A. Belov, Y. S. Kivshar, *Phys. Rev. Lett.* **2015**, 114, 123901.
- [15] C. Poli, M. Bellec, U. Kuhl, F. Mortessane, H. Schomerus, *Nat. Commun.* **2015**, 6, 6710.
- [16] H. Zhao, P. Miao, M. H. Teimourpour, S. Malzard, R. El-Ganainy, H. Schomerus, L. Feng, *Nat. Commun.* **2018**, 9, 981.
- [17] M. Hafezi, E. A. Demler, M. D. Lukin, J. M. Taylor, *Nat. Phys.* **2011**, 7, 907.
- [18] Y. Guo, M. Xiao, S. Fan, *Phys. Rev. Lett.* **2017**, 119, 167401.
- [19] Q. Lin, M. Xiao, L. Yuan, S. Fan, *Nat. Commun.* **2016**, 7, 13731.
- [20] S. Kruk, A. Poddubny, D. Smirnova, L. Wang, A. Slobozhanyuk, A. Shorokhov, I. Kravchenko, B. Luther-Davies, Y. Kivshar, *Nat. Nanotechnol.* **2019**, 14, 126.
- [21] G. Harari, M. A. Bandres, Y. Lumer, M. C. Rechtsman, Y. D. Chong, M. Khajavikhan, D. N. Christodoulides, M. Segev, *Science* **2018**, 359, eaar4003.
- [22] M. A. Bandres, S. Wittek, G. Harari, M. Parto, J. Ren, M. Segev, D. N. Christodoulides, M. Khajavikhan, *Science* **2018**, 359, eaar4005.
- [23] S. E. Miller, *Bell Syst. Tech. J.* **1969**, 48, 2059.
- [24] V. S. Y. Lin, K. Moteshareei, K.-P. S. Dancil, M. J. Sailor, M. R. Ghadiri, *Science* **1997**, 278, 840.
- [25] B. Jalali, S. Fathpour, *J. Lightwave Technol.* **2006**, 24, 4600.
- [26] V. R. Almeida, C. A. Barrios, R. R. Panepucci, M. Lipson, *Nature* **2004**, 431, 1081.
- [27] Q. Xu, B. Schmidt, S. Pradhan, M. Lipson, *Nature* **2005**, 435, 325.
- [28] D. Dai, Z. Wang, J. E. Bowers, *Opt. Lett.* **2011**, 36, 2590.
- [29] D. Dai, J. Bauters, J. E. Bowers, *Light: Sci. Appl.* **2012**, 1, e1.
- [30] E. A. J. Marcatili, *Bell Syst. Tech. J.* **1969**, 48, 2071.
- [31] H. Yamada, T. Chu, S. Ishida, Y. Arakawa, *IEEE Photonics Technol. Lett.* **2005**, 17, 585.
- [32] M. Born, E. Wolf, *Principles of Optics*, Cambridge University Press, Cambridge, UK **1999**.
- [33] X. Chen, M. M. Milosevic, A. F. J. Runge, X. Yu, A. Z. Khokhar, S. Mailis, D. J. Thomson, A. C. Peacock, S. Saito, G. T. Reed, arXiv: 1807.01656 [physics.app-ph], **2018**.
- [34] H. Oukraoui, V. Coda, A. A. Rangelov, G. Montemezzani, *Phys. Rev. A* **2018**, 97, 023811.
- [35] T. Lunghi, F. Dautre, A. P. Rambau, M. Bellec, M. P. De Micheli, A. M. Apetrei, O. Alibart, N. Belabas, S. Tascu, S. Tanzilli, *Opt. Express* **2018**, 26, 27058.
- [36] R. Menchon-Enrich, A. Llobera, V. J. Cadarso, J. Mompart, V. Ahufinger, *IEEE Photonics Technol. Lett.* **2012**, 24, 536.
- [37] R. Menchon-Enrich, A. Llobera, J. Vila-Planas, V. J. Cadarso, J. Mompart, V. Ahufinger, *Light: Sci. Appl.* **2013**, 2, e90.
- [38] M. I. Shalae, W. Walasik, A. Tsukernik, Y. Xu, N. M. Litchinitser, *Nat. Nanotechnol.* **2019**, 14, 31.
- [39] X. T. He, E. T. Liang, J. J. Yuan, H. Y. Qiu, X. D. Chen, F. L. Zhao, J. W. Dong, *Nat. Commun.* **2019**, 10, 872.
- [40] P. Delplace, D. Ullmo, G. Montambaux, *Phys. Rev. B* **2011**, 84, 195452.
- [41] J. Zak, *Phys. Rev. Lett.* **1989**, 62, 2747.
- [42] S. Ryu, Y. Hatsugai, *Phys. Rev. Lett.* **2002**, 89, 077002.
- [43] A. Poddubny, A. Miroshnichenko, A. Slobozhanyuk, Y. Kivshar, *ACS Photonics* **2014**, 1, 101.